Carbon Trends 13 (2023) 100310

Contents lists available at ScienceDirect

Carbon Trends

journal homepage: www.elsevier.com/locate/cartre

New local pseudopotential for multilayer carbon materials and its application in wave packet dynamics

Géza I. Márk [a,*], Péter Vancsó [a], Alexandre Mayer [b]

[a] Institute for Technical Physics and Materials Science, Centre for Energy Research, 1121 Budapest, Hungary
[b] Department of Physics, University of Namur, 5000, Namur, Belgium

ARTICLE INFO

Keywords:
Graphene
Graphite
Bilayer graphene
Rhombohedral graphene
Wave packet dynamics
Pseudopotential
Band structure
Tight-binding

ABSTRACT

Formerly we created a one-electron local pseudopotential which proved to be successful in studying transport phenomena in various sp^2 carbon nanosystems, e.g. graphene grain boundaries and nanotube networks. In this work, we present an extended version of the local pseudopotential which correctly describes the electronic structure of van der Waals stacks of carbon sheets, e.g. AA, AB bi-layer graphene, ABC (rhombohedral) tri-layer graphene, as well as AA, AB, and ABC graphite, etc., even in case of external electric fields. We utilize this potential to study the hopping dynamics of wave packets between the graphene sheets in multilayer systems. The frequency of the hopping is proportional to the band splitting, caused by the interlayer coupling. For the case of AB and ABC graphene there is a backscattering near the Fermi level, causing a Zitterbewegung-like phenomenon, an interference between $+k_{Bloch}$ and $-k_{Bloch}$ states. For the rhombohedral tri-layer graphene the time dependence of the wave packet probability density is an aperiodic function for the first- and third layer (the two outer layers), but a quasi-periodic function for the second (inner) layer.

1. Introduction

Layered materials [1] are composed of two-dimensional (2D) sheets, where the intra-layer bonds (those between adjacent atoms inside the 2D sheet) are strong, covalent bonds, but the inter-layer bonds (those between atoms in adjacent layers) are weak, van der Waals bonds. Even when the single 2D layers have the same structure, the three-dimensional (3D) structure built from them can have (infinitely) many variations, depending on the number [2], orientation [3], and displacement of the individual layers. The electronic structure and transport properties of the 3D stacks strongly depend on these factors. In the recent years experimentalists learned how to control these parameters and explored many interesting phenomena. These include topological edge states [4], charge density waves [5,6], Mott-insulator phases [7], etc. These heterostructures have potential industrial applications as transistors [8], photodetectors [9,10], photovoltaics [11], sensors [12], and batteries [13].

Most of this work was devoted to multilayer structures built from different 2D materials. In this field, however, a special attention is being paid to multilayers composed of graphene sheets only. Recent experiments highlight that the electronic structure of multilayer carbon materials also shows a multitude of features, including superconductivity [14] in twisted bilayers, quantum magnetism [15], and topological phenomena [16] in rhombohedral stacking, etc.

The theoretical treatment of multilayer carbon materials, however, is challenging. For example, in the case of twisted bilayer graphene [3], the interesting physics occurs for small, "magic" angles [14,17], but the very large unit cell of such moiré systems makes it difficult to use ab-initio methods. This is also true for the practically important case of multilayer carbon structures containing structural defects [18,19].

Wave packet dynamics (WPD) [20] calculations can handle realistic models containing tens of thousands of atoms even on a personal computer. WPD also treats the structural defects quite well [21] because it can simulate electronic dynamics including multiple scattering processes at the nanoscale. In WPD modeling the physical system is described by a Hamiltonian and the initial conditions are given by an initial wave function. The method provides the $\psi(\vec{r},t)$ time-dependent wave function by the solution of the time-dependent Schrödinger equation. The $\psi(\vec{r},E)$ energy-dependent wave function is also available through the time-energy Fourier transform. Studying the details of the time-dependent wave function helps us to understand dynamic processes, e.g. those occurring in a Scanning Tunneling Microscope (STM)

* Corresponding author.
E-mail address: mark.geza@ek.hun-ren.hu (G.I. Márk).

https://doi.org/10.1016/j.cartre.2023.100310
Received 28 July 2023; Received in revised form 27 October 2023; Accepted 31 October 2023
Available online 3 November 2023

[22] and the energy-dependent wave function makes it possible to explain the quasiparticle interferences (QPIs) [23] seen around the defects in STM. In the one (quasi)particle approximation, only a one particle 3D wave function is calculated instead of the many-body wave function and the details of the many-body interactions are hidden in the Hamilton operator. The details of the many-body electronic structure can be coded either in the kinetic energy part [23], or in the potential energy part of the Hamiltonian. In the simplest approximation the kinetic energy operator is identical to the free space kinetic energy of the electron $(-k^2/2)$ and the many-body electronic structure is coded into a local one electron pseudopotential $V(\vec{r})$. Another widely used formulation of WPD when the Hamilton operator is expressed in a tight-binding (TB) approximation [24], however, in this method the TB parameters need to be optimized for each stacking geometry and also for the specific defect types.

The problem of determining the $V(\vec{r})$ one-electron pseudopotential which yields a given electronic band structure, i.e. a given $E(\vec{k}_{Bloch})$ dispersion relation is called the band structure inverse problem and an approximate solution can be given, e.g., by variational methods. Formerly we developed such a local one-electron pseudopotential [25] for graphene and applied it to many sp^2 carbon nanosystems [22,26]. This considers both the specific geometrical arrangement of the carbon atoms (hexagonal lattice) and the specific electronic structure of graphene (linear dispersion near the *K* points for electrons near the Fermi energy (E_F), trigonal warping for hot electrons, etc.). It also allows to handle localized defects and we utilized this feature of the pseudopotential in calculating the transport properties of different 0D and 1D graphene defects [27,21], such as different graphene grain boundaries.

The old pseudopotential correctly described planar graphene structures, even in case of curved planes, however, did not take into account the van der Waals interaction between the graphene sheets. Indeed, the band structure calculated with that potential shows no dispersion in the K-H direction (direction perpendicular to the graphene sheet in reciprocal space, see Fig. 2.inset for the points in the Brillouin zone). In order to handle multilayer systems, we created a new pseudopotential which corrects these problems. We present the construction and some applications of this new pseudopotential in this paper.

The organization of the paper is as follows. The new, anisotropic pseudopotential is introduced in Section II. In Section III we calculate the plane-wave band structure for characteristic bi-layer, tri-layer, and infinite layer graphene stacks with the new pseudopotential. In Section IV we explain the setup of the WPD calculations, analyze and discuss the results for AA and AB bi-layer graphene in the time-domain and in the energy-domain. An application of the pseudopotential for tri-layer rhombohedral graphene is presented in Section V. Section VI is devoted to conclusions.

Hartree atomic units are used in all formulas except where explicit units are given. SI units are used, however, in all the figures and numerical data. All energy values are relative to the vacuum level, unless otherwise stated.

2. Construction of the pseudopotential

Our formerly developed one electron local pseudopotential [25] was constructed as a sum of radial symmetric functions centered on each carbon atoms. The radial symmetric functions were themselves a sum of three Gaussians with different amplitudes and widths. Hence the old potential had six parameters (apart from the given atomic coordinates): the A_j amplitudes and the a_j widths ($j = 1,2,3$). The band structure depends on these six parameters and on the atomic positions:

$$E_n\left(\vec{k}_{Bloch};\left\{A_j,a_j\right\}_{j=1}^{3},\left\{\vec{r}_i\right\}_{i=1}^{N}\right)=F\left[V\left(\vec{r};\left\{A_j,a_j\right\}_{j=1}^{3},\left\{\vec{r}_i\right\}_{i=1}^{N}\right)\right]$$

We provided an approximate solution of the band structure inverse problem by variationally matching the lowest two bands calculated by the plane wave procedure with the π bands of the graphene sheet, using a TB approximation [25]. Formerly we used this potential in the WPD calculations for the planar (and slightly curved) carbon nanosystems.

If, however, we calculate not only the dispersion relation, but the Bloch wave functions also [23], we can see that the lowest two bands obtained by the above mentioned procedure have a σ character, with wave functions centered on the atomic sites, and having a maximum of the probability density in the graphene sheet. Sigma wave functions describe well the C—C bonds, but σ wave functions of two neighboring graphene sheets have only a negligible overlap because of the large interlayer distance. Hence, in order to describe the interlayer interactions correctly, we have to switch to the π bands. Pi orbitals of adjacent sheets can have a sizeable overlap, thanks to the p_z character of the π orbitals. From the algorithmic point of view this simply means that instead of the lowest two bands we must concentrate on those bands giving π character wave functions and utilize these bands in the variational optimization.

The approach used to determine the new pseudopotential is like that applied in our previous work [25]. We consider TB reference data for the band structure of isolated graphene sheets and AA graphite. We use in this work TB models that rely on *s*, p_x, p_y and p_z orbitals (in contrast with TB models based on π orbitals in our previous work). These models provide band structures with eight energy levels $E_n(k_{Bloch})$ for each value of the wavevector k_{Bloch} (in contrast with 2 energy levels). A local pseudopotential is then constructed so that the energy bands provided by a plane-wave calculation match as closely as possible the π bands provided by the TB model in an energy window of ± 3 eV around the Fermi level. As a further refinement to the potential, we use 4 Gaussians, with adjustable width and amplitude parameters and the new potential has different planar- and perpendicular parameters. In contrast, the pseudopotential developed in our previous work consisted of only 3 Gaussians with isotropic parameters. The details of the fitting procedure are given in Supplement 1. The functional form of the new pseudopotential is given by

$$V\left(\vec{r};\left\{A_j,a_{planar,j},a_{perp,j}\right\}_{j=1}^{4},\left\{\vec{r}_i\right\}_{i=1}^{N}\right)=\sum_{i=1}^{N}\sum_{j=1}^{4}A_j e^{-\left[a_{planar,j}\left(x-r_{x,i}\right)^2+a_{planar,j}\left(y-r_{y,i}\right)^2+a_{perp,j}\left(z-r_{z,i}\right)^2\right]}$$

where the 12 parameters $\{A_j,a_{planar,j},a_{perp,j}\}_{j=1}^{4}$ must be adjusted in order to achieve the best possible agreement with the TB reference data for the π bands of graphene and AA graphite around the Fermi level. This was achieved by defining a fitness function for quantifying the difference between the energy bands provided by the TB and the plane-wave

Table 1
Parameters of the new anisotropic local pseudopotential for carbon atoms in graphene and graphite.

	A_j (eV)	$a_{planar,j}$ (r_{Bohr}^{-2})	$a_{perp,j}$ (r_{Bohr}^{-2})
Gaussian #1	−84.6841	1.00316	0.27752
Gaussian #2	120.6472	2.51913	2.29511
Gaussian #3	142.2017	2.44581	2.92539
Gaussian #4	−73.3189	0.56255	1.32379

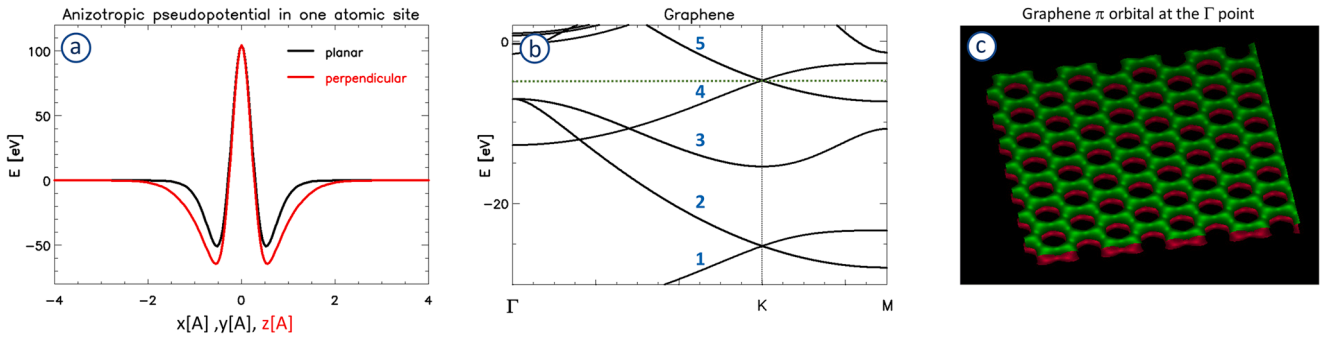

Fig. 1. Construction of the local one-electron anisotropic pseudopotential. (a) Planar- and perpendicular linecuts of the optimized $V(\vec{r})$ pseudopotential applied to a single atomic site at the origin. (b) Plane wave band structure calculated for a single-layer graphene surface. (c) Shape of the π orbitals (band 4) in the Γ point. Green and red are the positive and negative lobes of the wave function.

techniques (the fitness function gives more weight to the parts of the band structure that are the most important, here the Γ, K, M and H points for energy values in an energy window of ±3 eV around the Fermi level). The fitness function is then minimized by using a Monte Carlo technique. The parameters obtained by this approach are given in Table 1.

After the variational optimization of the pseudopotential, we can see (Fig. 1a) that the resulting potential is indeed anisotropic. Fig. 1b and c shows that the optimization criteria were indeed met: (i) the π bands (band 4 and 5) match with the TB π band of graphene and (ii) the Z dependence of the wave functions of these bands have indeed a π

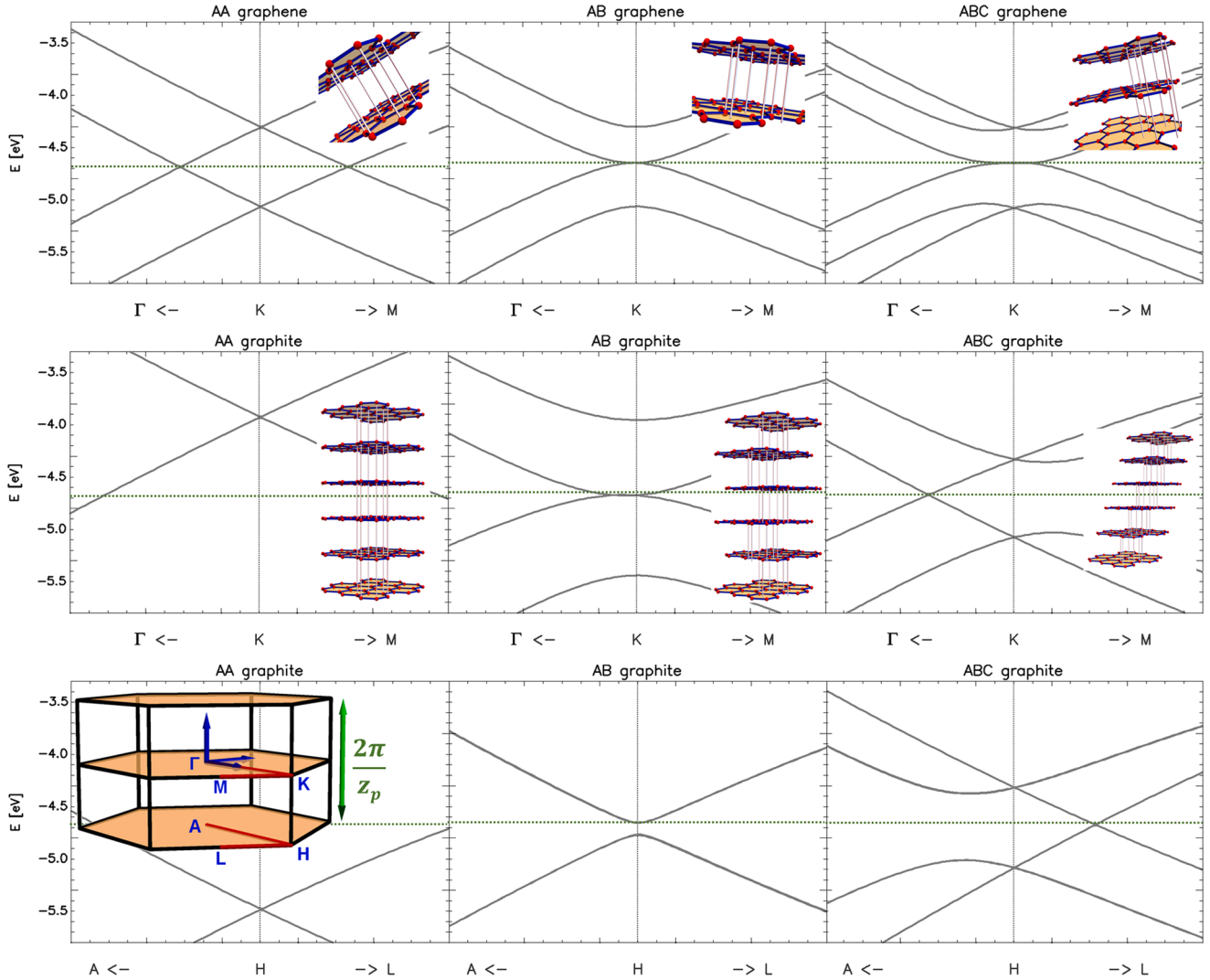

Fig. 2. Plane-wave low energy π band structures for various few-layer and bulk multilayer carbon structures. (Upper row) AA bi-layer, AB bi-layer, and ABC tri-layer. (Middle row) AA, AB, and ABC infinite layer for k_z=0. (Lower row) AA, AB, and ABC infinite layer for $k_z^{max} = \pi/z_p$. The energy scale is the same in all subfigures. The green dotted horizontal lines show the position of the Fermi energy. The insets show the stacking order of the layers. The interlayer distance is chosen to be $c = 3.46$ A for all systems (see the text for details). The inset in the lower left subfigure shows the graphite Brillouin zone. The blue coordinate axes are the $\{k_x,k_y,k_z\}$ vectors, the red lines show the Γ-K-M and A-H-L paths, along which the band structures were calculated. The z_p period is c for single-layer graphite, 2c for AA and AB graphite and 3c for ABC graphite.

character – there is a zero-probability density node-plane in the graphene plane and the maxima of the probability density are at 0.7 Angström above- and below the graphene sheet, in good agreement with DFT results [28]. The linear π and $\pi^{'}$ bands cross each other at the K point at E_F=−4.68 eV.

3. Verification of the pseudopotential

Bulk graphite consists of periodically stacked graphene layers. There are three kinds of ordered graphite configurations: the simple hexagonal graphite (the AA-stacked graphite), the Bernal graphite (the AB-stacked graphite), and the rhombohedral graphite (the ABC-stacked graphite) [29]. The few(est)-layer versions of these structures are the bi-layer graphene with AA and AB configurations and the tri-layer graphene with ABC configuration. The band structure of all these systems were studied extensively, both experimentally and theoretically. Hence, we choose these models to verify the performance of the new pseudopotential for multilayer systems.

Fig. 2. shows the π band structures numerically calculated with the anisotropic pseudopotential using the reciprocal space plane-wave method for few-layer and infinite layer carbon systems. According to geometry optimized ab-initio calculations the interlayer distance c does depend on the stacking, but the precise distances vary with the specific DFT functional. We chose a fixed $c = 3.46\ A$ interlayer distance in the present paper [30], as an average for the different geometries considered, in order to focus only on the effect [31] of the symmetry and stacking on the band structure. These band structures nicely reproduce the ab-initio results for the corresponding systems for all of the cases analyzed (apart from the slightly different gaps due to the fixed interlayer distance), not only for the k_z=0 case (middle row of Fig. 2), but also for the $k_z^{max} = \pi/z_p$ case (lower row of Fig. 2), where z_p is the Z periodicity of the infinite-layer structure, $z_p = c$, $2c$, and $3c$ for the AA, AB, and ABC graphites, respectively. The KH shift (compare the middle- and lower rows of Fig. 2) is decreasing with increasing z_p.

As we demonstrate in Fig. 3. the pseudopotential correctly describes such fine details of the band structure as the small band gap of the rhombohedral graphene and even the increasing of this band gap when applying a perpendicular electric field. This latter result was calculated by adding a linear electrostatic potential, $E(z) = e\ E_z z$ to the pseudopotential, where $E_z = 0.035\ V/A$ is the electric field, which corresponds to a 0.2 V/A bias, considering the effect of the screening [32].

4. Wave packet dynamical calculations – Test systems – AA and AB bi-layer graphene

In our earlier paper [23] we calculated the propagation of quasi-particle wave packets (WPs) on a single-layer graphene surface. This was accomplished in three steps. First, we numerically calculated the Bloch wave functions of the graphene sheet, by numerically solving the stationary Schrödinger equation for each k_{Bloch} Bloch wave vectors in the Brillouin zone. The graphene sheet was modelled with the lattice periodic (old) pseudopotential. Then a Bloch WP was constructed by integrating in $\{k_x, k_y\}$ over the 2D Brillouin zone utilizing a Gaussian weight function. Finally, the time development of this initial state was calculated by numerically solving the time dependent Schrödinger equation, utilizing again the pseudopotential. See Supplement 2 for details. Time dependent measurable quantities, such as probability densities and probability currents were directly calculated from the time dependent wave function. Moreover, after a time—energy Fourier transform, energy dependent measurables became also available. For example, when the WP is centered on a K point and the energy spread of the WP is small, the WP propagates on the graphene surface with velocity v_F(Fermi velocity) with a very small dispersion, because the dispersion relation is linear near the K point.

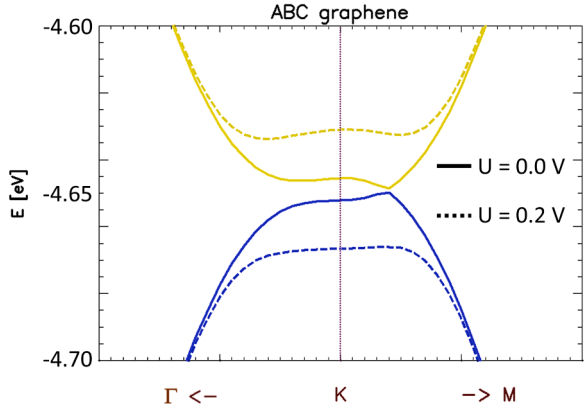

Fig. 3. Zoomed-in detail of the band structure for the rhombohedral graphene. The solid curve is for no bias and the dashed curve is for a 0.2 V/A bias.

In this paper we extend this scheme for multilayer carbon systems. First, we calculate the Bloch states for a pristine single-layer graphene sheet with the new anisotropic pseudopotential and construct the Bloch WP from these states. Then we create a model system (Fig. 4a) consisting of two regions: (1) a single-layer region and (2) a multiple-layer region (two-layer in this figure). The system is infinite (periodic) in the x direction (parallel to the boundary of the two regions) but the graphene sheets in Region (2) can have different distances, displacements, and rotations relative to each other to simulate several graphene multilayer geometries. The WP starts from Region (1) then it propagates into Region (2). The initial impulse of the WP is perpendicular to the boundary (y) and its width is infinite in the direction parallel to the boundary (x), i.e. $\vec{p} = p_y \vec{y}$.

When the WP enters into Region (2), it begins to feel the van der Waals potential of the second graphene sheet. Because of this perturbation potential the momentum distribution won't anymore remain constant – the Bloch functions of the single-layer graphene are not anymore eigenstates of the two-layer system. As a result, the WP will slowly tunnel back and forth between the two layers, similar to the alternating oscillation in a classical coupled pendulums system (Fig. 4b, c). Similarly to the classical example, the coupling strength determines the frequency of the hopping: the stronger the coupling (k), the larger the frequency of the hopping. Indeed, as we see in Fig. 4d,e, the single-layer graphene bands split into two bands on the bi-layer AA graphene and the Δk magnitude of this splitting determines the hopping frequency between the layers at a given energy value.

Fig. 4. illustrates the simplest case, the AA bi-layer graphene. In this case the behavior of the WP is rather uneventful, the magnitude of the Δk splitting of the bands only changes a little in our investigated energy window (see Fig. 6 for details). The case of AB bi-layer graphene and ABC tri-layer graphene is more interesting, giving rise to backscattering, Zitterbewegung-like phenomena, aperiodic and periodic hopping, etc. We will examine these phenomena in the remaining portion of this Section and the next Section.

Fig. 5. shows the time development of the WP for AA and AB bi-layer graphene, where (a) is the schematical y-z cross section (side view) of the geometry. The system is infinite in the x direction (see Fig. 4a for the coordinate system). Fig. 4b and c show the potential and the time development of the WP for the AA and AB bi-layer graphene in a "shifted top view" mode, meaning that we display the two layers (a thin ribbon cut from each of them) under each other. Fig. 5d, however, shows the whole 3D WP (for a slightly wider ribbon) by a 3D isoprobability-density surface. Note the π character of the orbitals in this figure: the isodensity surface has two layers of maxima below- and above both graphene sheets, corresponding to the two (positive and negative) lobes of the wave function (Fig. 1c). The isodensity surfaces are composed of closed 3D objects (around the local maxima of the wave function) with nearly spherical shapes. In Region (1) (left part of the figure) there is only one

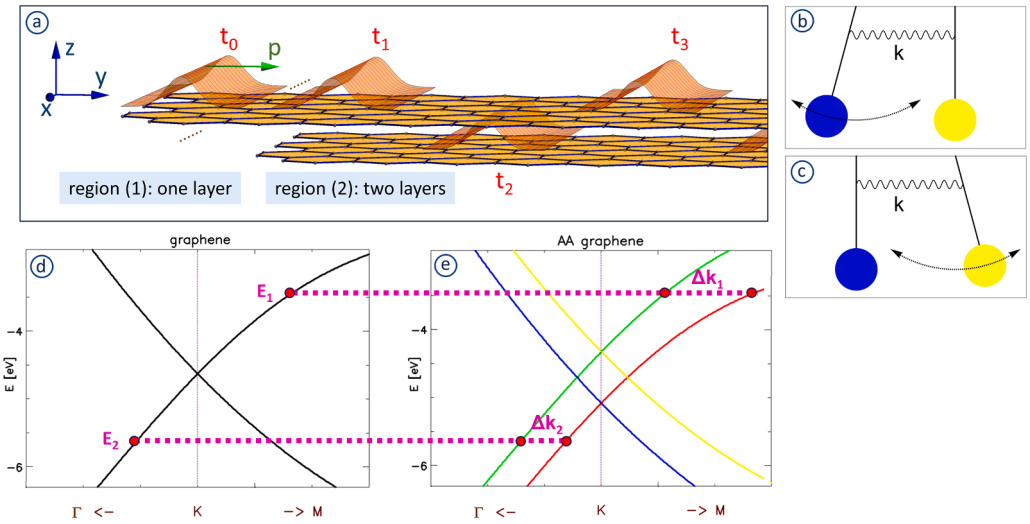

Fig. 4. Schematics of the wave packet dynamical calculation for AA (simple hexagonal) two-layer graphene. (a) Region (1) contains one graphene layer, Region (2) contains two graphene layers. The Bloch wave packet starts at time $t = t_0$ from Region (1) with an impulse p perpendicular to the boundary. The system is infinite in the x direction (see the brown dots near t_0 in "a"). As the wave packet moves in the y direction it begins to hop between the two graphene layers, as the schematical figure shows its position at times t_1, t_2, and t_3. The figure is not to scale. (b,c) Classical physics illustration: the oscillation alternates between the two pendulums, coupled with a weak spring of spring constant k. (d,e) Splitting of the graphene bands when the wave packet enters from the single-layer region (Region (1)) into the two-layer region (Region (2)). See the text for details.

graphene layer, therefore we can see only two sheets of maxima, but there are four sheets of maxima in Region (2). The probability density is changing in the y direction; hence the size of the isodensity "spheres" is also changing along this direction. In the case of the 2D images (b and c) we integrated the probability density in the z direction utilizing a Gaussian weight function centered on both graphene sheets.

At $t = 0$ fs the WP is localized on Layer 1 in Region (1) (Fig. 5b,c). Then it propagates into the $+y$ direction (vector P in Fig. 5a) towards the boundary. As we can see by comparing (b) and (c), the time development is markedly different for the AA and the AB stacking. In the case of the AA stacking the main phenomenon is the above mentioned back and forth tunneling between the two layers, but the AB case shows a much more complicated picture, see Fig. 5c lower pane ($t = 13.9$ fs): (i) there is a reflection at the boundary; (ii) the WP is broken into several parts in Region (2); and (iii) the atomical scale pattern of the WP is changing in time and space – see below for the explanation of these phenomena. Fig. 5d helps us to imagine the 3D structure of the WP. This displays the snapshot of the time development at $t = 13.9$ fs (see the video in Supplement 6 for the complete time development of the isodensity surface). At this particular time the WP is already present on both layers in Region (2) but a part of it is reflected back into Region (1).

As we can see in Fig. 5, the time development of the Bloch WPs occur in two distinct length scales: (i) there are changes on the atomic scale wave function (the "u" factor of the Bloch function) and (ii) there are changes on the 10 Angstrom scale (superpositions with different amplitudes and phases of the exponential factors of the Bloch functions with different k_{Bloch} values). The behavior of the Bloch WP in the two spatial scales are, however, not independent. For example, in the AA bi-graphene case (Fig. 5b) the atomic scale pattern of the WP seems to be unchanged during the time evolution (see also Fig. 2. in Ref [23]). The WP is constructed by summing the Bloch wave functions with a Gaussian centered on a K point and having a narrow momentum distribution. When this WP is evolving on a pristine graphene sheet, as in Region(1) of our Fig. 5, the Bloch-momentum distribution remains constant, but the phases of the components are slowly changing in time with different speeds, because the dispersion relation is not linear away from the K point, hence the width of the WP is slowly increasing – but this spreading is considerably slower than for a WP propagating in free space, where the dispersion relation is quadratic. When the WP enters into Region (2), in the case of AA graphene we do not see any backscattering at the boundary and the shape of the atomic patterns remains seemingly unchanged, which means that only intravalley scattering occurs in this case. The case of the AB graphene (Fig. 5c) is different. There is a considerable amount of backscattering at the Region (1–2) interface, this indicates the presence of intervalley scattering, the emergence of states at the opposite K point, which means a momentum in the opposite direction. Consistently with this observation, the atomic scale pattern is also changing, caused by the interference of the Bloch waves at the two opposite K valleys. It is worth noting that the observed effects are nearly the same if we inject the WP along armchair direction instead zigzag, because AA and AB bi-graphenes are isotropic near the K point in the investigated energy region.

In order to study the long-range behavior of the WP, we calculated space-time and space-energy WP probability density maps. The calculation method of the space-time density is given in detail in Supplement 3, together with the analysis of the results.

One single WPD calculation provides us with the behavior of all the energy components contained in the spectrum of the WP. By the help of the time-energy Fourier transform (see Supplement 2 for details) of the time dependent wave function, we can access these individual spectral components. Fig. 6. shows the long-range behavior of the different energy components of the WP on bi-layer graphene for the AA and AB stacking configurations as color coded space-energy density maps. The calculation of the $\varrho_{Layer\ l}(y,E)$ probability density is similar to the space-time density map (Supplement 3) but using the energy dependent wave functions $\psi(x,y,z,E)$ instead of the time dependent ones. $l = 1,2$ is the layer index. The normalization is performed by first calculating the $\varrho_{graphene}(y,E)$ density by performing a WPD run followed by a t-E FFT for a pristine graphene system then normalizing the two-layer probability with this function for each energy level:

$$\varrho^{normalized}_{Layer\ l}(y,E) = \varrho_{Layer\ l}(y,E) \Big/ \varrho_{graphene}(y,E).$$

The case of AA stacking (Fig. 6b,d,f) is relatively simple. The most important phenomenon seen on the (b) and (f) image is the oscillation of the WP between the two layers (alternation of the blue and yellow colors). The spatial period of this oscillation monotonously decreases with increasing energy. This decrease is consistent with the increasing k splitting of the AA bands, as seen on Fig. 6d, where we plotted the

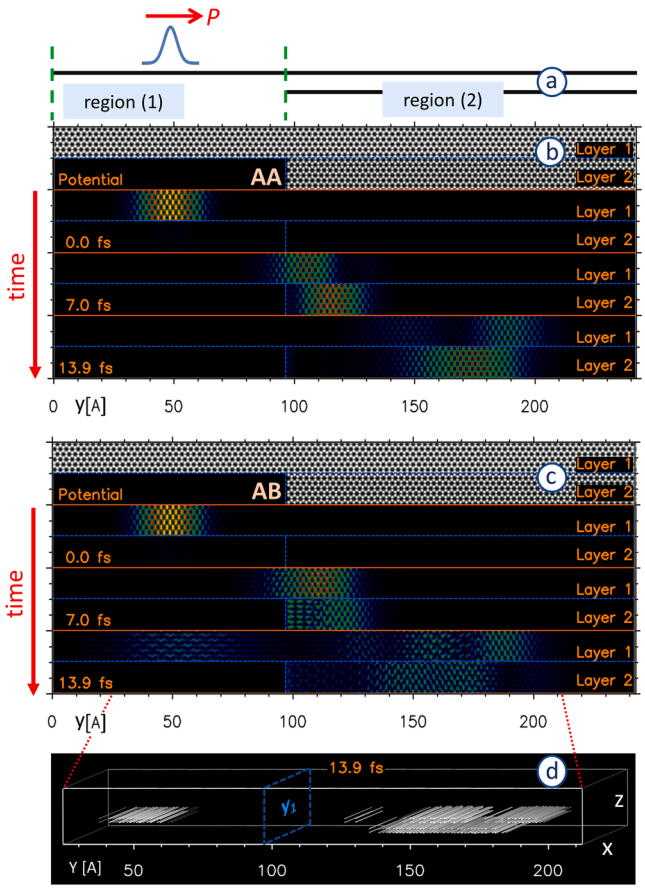

Fig. 5. Time dependent probability density of the wave packet in AA and AB bi-layer graphene. (a) Calculation scheme (side view). (b,c) Shifted top-view images (see the text for details) of the pseudopotential and the probability density in the two layers for (b) AA stacking and (c) AB stacking. (d) 3D isodensity surfaces of the probability density at $t = 13.9$ fs for the AB case, displayed on a slightly enlarged y scale (see the dotted red lines). The blue rectangle marked with y_1 shows the boundary of the two regions. See the video in Supplement 6 for the complete time development.

$$s(k_{Bloch};E) = \left|\left\langle \psi^{bi-layer}(\vec{r};E)|\varphi^{single-layer}_{k_{Bloch}}(\vec{r})\right\rangle\right|$$

absolute value of the scalar product of the two-layer graphene energy decomposed WP, with the Bloch wave functions $\varphi^{single-layer}_{k_{Bloch}}(\vec{r})$ of the single-layer graphene (a generalized Fourier transform), with $\vec{r} = (x,y,z)$. This $s(k_{Bloch};E)$ quantity basically reproduces the band structure of the AA and AB graphene (compare Fig. 2 and Fig. 6d,e), but the $-k_{\mathrm{Bloch}}$ bands (backscattering bands in our transport calculations) are not excited in the case of AA, however they are weakly excited in the case of AB in the vicinity of E_F. The two branches of the bi-layer graphene band structure mean that for any given energy E there are two slightly different k_{Bloch} values, i.e. a pair of wave functions with slightly different spatial freuencies. The interference of these pairs of wave functions gives the long range oscillation seen on Fig. 6b and f.

For the case of the AA graphene the $\Delta k(E)$ splitting monotonously increases in our [−5.8 eV – −3.3 eV] energy window. This explains the monotonous decrease of the hopping distance (i.e. the distance, where the oscillation between the two layers takes place) seen on Fig. 6b. In the space-energy density for the AB bi-layer graphene (Fig. 6c) the situation is similar in the energy region, where the second (parabolic) valance and conduction bands appear ([E<E8 *and* E>E4]): the $+k_{\mathrm{Bloch}}$ graphene band splits into two bands and $\Delta k(E)$ determines the hopping distance similar to the AA graphene. There is, however, a band crossing at −3.1 eV, $\Delta k = 0$ here and it slowly increases until the band edge (E4), hence the hopping distance is infinite at −3.1 eV and decreases until E4. By contrast, in the vicinity of the Fermi-level (between E4 and E8) there is only one $+k_{\mathrm{Bloch}}$ branch in Fig. 6e, but there is a weak $-k_{\mathrm{Bloch}}$ branch (shown in red). In this energy region, the interference of these states determines the hopping between the layers. We can observe two features here: (i) $\Delta k(E)$ decreases (to zero) when approaching E_F=E6 from either below or above, hence the hopping distance diverges when approaching E_F and (ii) the amplitude of the hopping is small (see the line cuts at Fig. 6g for E5 and E7), because the $-k_{\mathrm{Bloch}}$ components of the WP have a considerably smaller amplitude than the $+k_{\mathrm{Bloch}}$ components. These weak oscillations are similar to the Zitterbewegung motion [33], where positive- and negative energy wavefunctions interfere. The two parabolic bands meet at EF=E6; hence the band structure is locally flat at this point. As we can see on Fig. 6c and g, there is a considerable amount of WP reflection on this energy level, as shown by the large probability to the left of y_0, seen as a blue bar on c6 and a finite intensity on g6 – since y_0 is the point from where the WP started, the presence of a finite WP probability to the left of this point signifies a reflection. At this energy level the WP can tunnel into Region (II) but can not propagate there, because of the zero value of the group velocity. Note the linear decay of the probability at g6. There are also some edge states seen in both the AA and AB calculations (E2 for AA and E1, E3 for AB), represented as black spots in Fig. 6b, c at y_1 (Region 1–2 boundary) and the large probability density is high-clipped at the point y_1 on Fig. 6g. The edge states cause strong forward- and backward scattering, seen as interference oscillations at these energy levels on the space-energy density map, even on the left side of y_0 (the starting position of the WP). We note that the new pseudopotential is not fitted for the different edge states of the graphene, therefore it is not yet suitable for a quantitative study of the effect of the edges on the transport properties.

5. Application for tri-layer rhombohedral graphene

After gaining some confidence from the good performance of the new pseudopotential for the AA and AB bi-layer graphene, we go on to explore WPD on ABC rhombohedral tri-layer graphene. Rhombohedral graphite features a staggered intra- and interlayer hopping pattern [2], similar to a one-dimensional (1D) Su-Schrieffer-Heeger (SSH) model [34]. This hopping pattern results in a flat electronic band and increased charge density on the surface at the Fermi-level. Recent transport [16] and STM measurements [15] in thick samples revealed strong correlation effects, gives the opportunity to investigate many-body physics in a simple graphite crystal. Investigating electron dynamics by using WPD in ABC tri-layer graphene can be the first step to reveal the complex behavior of the electrons in thick samples.

As we can see on Fig. 2, the band structure of this material is complex, having a flat band at E_F and two parabolic conduction and valance bands with band edges a little away in momentum from the K point (resulting in total 3 bands away from the Fermi-level). We performed a WPD calculation followed by a t-E Fourier transform for the ABC graphene in a similar setup as for AA and AB, just the Region 2 now has three graphene layers instead of two, each displaced relative to the next in an ABC configuration. Fig. 7b shows the long-range behavior of the different energy components of the WP, i.e. the $\varrho^{normalized}_{Layer\ l}(y,E)$ functions for (l = 1,2,3) as a color coded position-energy map. We utilized the Cyan-Magenta-Yellow subtractive color system (Supplement 4), each *(y, E)* pixel is colored cyan, magenta, and yellow, when the WP is on Layer 1,2, and 3, respectively – see Fig. 7c for the illustration of this color system. Fig. 7d shows the $\varrho_{1,2,3}(y)$ probability densities at fixed energies, marked E1 and E2 on "b" – these two energies are in the region, where all the 3 bands exist (i.e. above- and below the energy region, where only the flat band occur).

Note that while $\varrho_2(y)$, the probability density for the middle layer is a periodic function (magenta curve in Fig. 7d), $\varrho_{1,3}(y)$, the probability densities for the upper- and lower layers are not periodic (cyan and

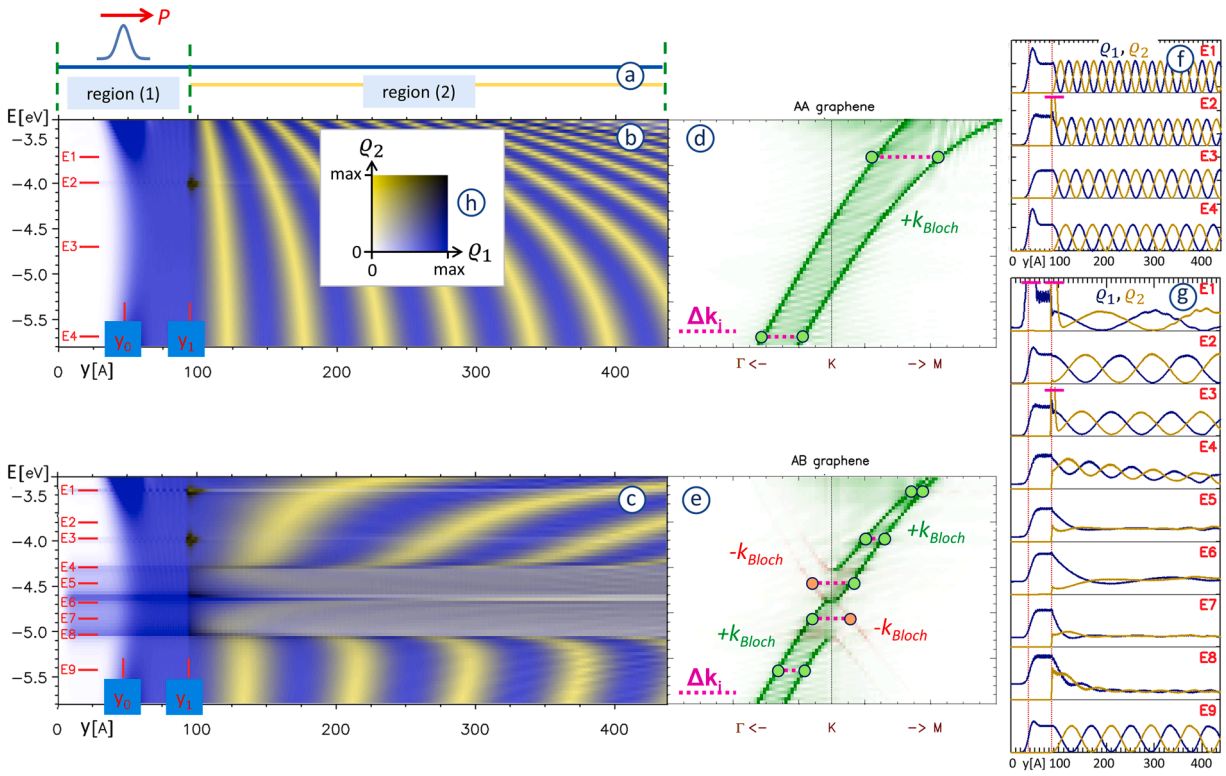

Fig. 6. Long-range energy-domain behavior of the wave packet on two-layer graphene. (a) is the calculation scheme, with the two graphene layers (side view, shown in blue and yellow). The wave packet starts from Region (1) at y_0 then propagates into Region (2) at y_1. (b,c) Color coded space-energy density map $\varrho(y,E)$ for AA and AB graphene, blue is for Layer 1, yellow is for Layer 2. The $E_i$red lines show characteristic energy levels. (d,e) Decomposition of the $\psi(x,y,z,E)$ two-layer wave functions in terms of the single-layer graphene Bloch states (see the text for details). Green is for positive $+k_{Bloch}$ (forward motion), red is for $-k_{Bloch}$ (backward scattering). The magenta broken lines show the Δk band splitting for different energy levels. (f,g) Position dependent wave packet probability densities $\varrho(y;E)$ for the two layers at different energy levels (marked in "b" and "c"), horizontal line cuts of (b,c). The Fermi level is at level "E3" in (b) and level "E6" in (c). Blue is for Layer 1, yellow is for Layer 2. The vertical dotted lines show the points y_0 (where the wave packet starts from) and y_1 (the Region 1–2 boundary). The normalization is the same at all curves. Magenta horizontal lines at (f2) and (g1,3) show the positions where the curves were high-clipped (localized states). (h) Color map.

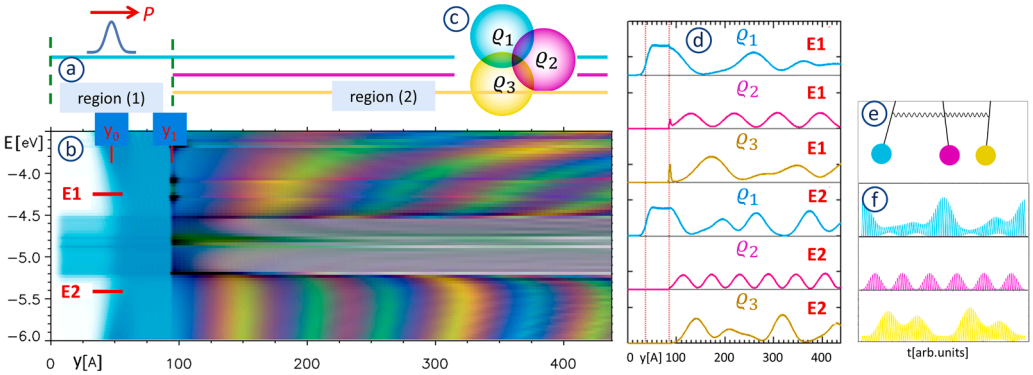

Fig. 7. Long-range energy-domain behavior of the wave packet on three-layer rhombohedral graphene. (a) is the calculation scheme, with the three graphene layers in ABC configuration (side view, shown in cyan, magenta, and yellow). The wave packet starts from Region (1) at y_0 then propagates into Region (2) at y_1. (b) CMY color coded space-energy density map $\varrho(y,E)$ for ABC graphene, cyan, magenta, and yellow are for Layer 1, 2, and 3, respectively. (c) Schematics of the cyan-magenta-yellow subtractive color system. (d) Position dependent wave packet probability densities $\varrho(y;E)$ for the three layers at E1 and E2 energy levels (marked in "b"). Cyan, magenta, and yellow are for Layer 1, 2, and 3, respectively. The vertical dotted lines show the points y_0 and y_1. The normalization is the same at all curves. (e) Three coupled pendulum model. (f) Oscillations of the three pendulum model (squared amplitudes).

yellow curves in Fig. 7d). We can understand this dynamical phenomenon by the help of a simple classical analogue – the three weakly coupled mathematical pendulums, Fig. 7e. The dynamical behavior of that system is indeed similar to the tri-layer graphene, because in both cases we have three identical oscillators coupled by a weak interaction potential. As we show in Supplement 5, in the three coupled pendulum case we have three incommensurate eigenfrequencies. That's why the motion of the two side pendulums is aperiodic. But the three corresponding eigenvectors are such that for the case of the middle pendulum, one of the eigenvectors have a zero component, hence for the middle pendulum we have only two eigenfrequencies that can interfere – this is the cause of the quasi-periodic motion of the second pendulum. The precise time dependence of the motion depends on the strength of the coupling and the relative amplitudes and phases used in the

superposition of the three eigenvectors, but already without a detailed fitting we can see, by comparing Fig. 7d and f, that the functions describing the two dynamical systems are indeed similar. Finally, we note that the flat band has an anisotropic behavior in k-space, therefore the WP propagation is different in the armchair and zigzag direction at the Fermi-level in contrast to AA and AB graphene cases. The investigation of this effect requires fine energy resolution in the calculations, since the band width of the flat band is around ~10 meV and beyond the scope of the present paper.

6. Conclusions

In this work, we presented the construction and a few applications of a local pseudopotential developed for van der Waals stacks of carbon sheets. It correctly describes the electronic structure of AA, AB bi-layer graphene, ABC (rhombohedral) tri-layer graphene, as well as AA, AB, and ABC graphite, even in case of external electric fields. By calculating the time development of quasiparticle WPs we studied the hopping dynamics between the graphene sheets in two- and three layer systems. The frequency of the hopping is proportional to the splitting of the graphene bands, caused by the interlayer coupling. For the case of AB and ABC graphene there is a backscattering near the Fermi level, causing a similar phenomenon as Zitterbewegung, an interference between $+k_{Bloch}$and $-k_{Bloch}$ states. For the rhombohedral tri-layer graphene the time dependence of the WP probability density is an aperiodic function for the first- and third layer (the two outer layers), but a quasi-periodic function for the second (inner) layer. This behavior was explained by a simple model, treating the electronic states of the adjacent graphene sheets as weakly coupled linear oscillators and noting that in case of the two outer layers the oscillation is characterized by three incommensurate frequencies but in case of the inner layer there are just two modes that can interfere. Similar long range hopping oscillations were seen in calculations for bilayer graphene [35], where the authors used it as a model of neutrino oscillations. Such long-range oscillations can in principle be measured, for example by Scanning Tunneling Microscopy, after creating standing waves by, for example, enclosing the multilayer graphene system in a potential well. Since the spatial period of the oscillation depends on the energy, such a system can select a specific energy range defined by the size of the potential well.

The pseudopotential presented in this paper can open new ways to investigate electron dynamics in moiré heterostructures, since WPD calculations can handle large unit cells with tens of thousands of atoms and thus resolve the bottleneck of the ab-initio calculations. We plan to study these moiré systems such as “magic-angle” bilayer graphene or stacking faults in rhombohedral graphite with the new pseudopotential as future work.

Declaration of Competing Interest

The authors declare that they have no known competing financial interests or personal relationships that could have appeared to influence the work reported in this paper.

Data availability

Data will be made available on request.

Acknowledgements

The work has been supported by the European H2020 Graphene Core3 project, Graphene Flagship, Grant No. 881603. G.I.M. and P.V. acknowledges support of the Fund for Scientific Research (FNRS) of Belgium. P.V. acknowledges support from the National Research, Development and Innovation Office (NKFIH) in Hungary, through Grant No. FK-142985. A.M. is funded by the Fund for Scientific Research (FNRS) of Belgium. He is member of the Namur Institute for Complex Systems (naXys). This research used resources of the “Plateforme Technologique de Calcul Intensif (PTCI)” located at the University of Namur, Belgium, which is supported by the FNRS under the convention No. 2.5020.11. The PTCI is member of the “Consortium des Equipements de Calcul Intensif (CECI)”. Helpful discussions with Ph. Lambin and P. Nemes-Incze are gratefully acknowledged.

Supplementary materials

Supplementary material associated with this article can be found, in the online version, at doi:10.1016/j.cartre.2023.100310.

References

[1] N. Mounet, M. Gibertini, P. Schwaller, D. Campi, A. Merkys, A. Marrazzo, T. Sohier, I.E. Castelli, A. Cepellotti, G. Pizzi, N. Marzari, Two-dimensional materials from high-throughput computational exfoliation of experimentally known compounds, Nat. Nanotechnol. 13 (2018) 246–252, https://doi.org/10.1038/s41565-017-0035-5.

[2] H. Min, A.H. MacDonald, Electronic structure of multilayer graphene, Progr. Theoret. Phys. Suppl. 176 (2008) 227–252, https://doi.org/10.1143/PTPS.176.227.

[3] S. Fang, E. Kaxiras, Electronic structure theory of weakly interacting bilayers, Phys. Rev. B 93 (2016), 235153, https://doi.org/10.1103/PhysRevB.93.235153.

[4] L. Kou, S.C. Wu, C. Felser, T. Frauenheim, C. Chen, B. Yan, Robust 2D topological insulators in van der Waals heterostructures, ACS Nano 8 (2014) 10448–10454, https://doi.org/10.1021/nn503789v.

[5] A.H. Castro Neto, Charge density wave, superconductivity, and anomalous metallic behavior in 2D transition metal dichalcogenides, Phys. Rev. Lett. 86 (2001) 4382–4385, https://doi.org/10.1103/PhysRevLett.86.4382.

[6] P. Dreher, W. Wan, A. Chikina, M. Bianchi, H. Guo, R. Harsh, S. Mañas-Valero, E. Coronado, A.J. Martínez-Galera, P. Hofmann, J.A. Miwa, M.M. Ugeda, Proximity effects on the charge density wave order and superconductivity in single-layer NbSe2, ACS Nano 15 (2021) 19430–19438, https://doi.org/10.1021/acsnano.1c06012.

[7] Z. Zhang, E.C. Regan, D. Wang, W. Zhao, S. Wang, M. Sayyad, K. Yumigeta, K. Watanabe, T. Taniguchi, S. Tongay, M. Crommie, M.P.Zaletel A.Zettl, F. Wang, Correlated interlayer exciton insulator in heterostructures of monolayer WSe2 and moiré WS2/WSe2, Nat. Phys. 18 (2022) 1214–1220, https://doi.org/10.1038/s41567-022-01702-z.

[8] L. Britnell, R.V. Gorbachev, R. Jalil, B.D. Belle, F. Schedin, A. Mishchenko, T. Georgiou, M.I. Katsnelson, L. Eaves, S.V. Morozov, N.M.R. Peres, J. Leist, A. K. Geim, K.S. Novoselov, L.A. Ponomarenko, Field-effect tunneling transistor based on vertical graphene heterostructures, Science 335 (2012) 947–950, https://doi.org/10.1126/science.1218461.

[9] A. Splendiani, L. Sun, Y. Zhang, T. Li, J. Kim, C.Y. Chim, G. Galli, F. Wang, Emerging photoluminescence in monolayer MoS2, Nano Lett 10 (2010) 1271–1275, https://doi.org/10.1021/nl903868w.

[10] Y. Chen, Y. Wang, Z. Wang, Y. Gu, Y. Ye, X. Chai, J. Ye, Y. Chen, R. Xie, Y. Zhou, Z. Hu, Q. Li, L. Zhang, F. Wang, P. Wang, J. Miao, J. Wang, X. Chen, W. Lu, P. Zhou, W. Hu, Unipolar barrier photodetectors based on van der Waals heterostructures, Nat. Electron 4 (2021) 357–363, https://doi.org/10.1038/s41928-021-00586-w.

[11] K.K. Paul, J.H. Kim, Y.H. Lee, Hot carrier photovoltaics in van der Waals heterostructures, Nat. Rev. Phys. 3 (2021) 178–192, https://doi.org/10.1038/s42254-020-00272-4.

[12] H.L. Hou, C. Anichini, P. Samorì, A. Criado, M. Prato, 2D Van der Waals heterostructures for chemical sensing, Adv. Funct. Mater. 32 (2022), 2207065, https://doi.org/10.1002/adfm.202207065.

[13] R. Rojaee, R. Shahbazian-Yassar, Two-dimensional materials to address the lithium battery challenges, ACS Nano 14 (2020) 2628–2658, https://doi.org/10.1021/acsnano.9b08396.

[14] Y. Cao, V. Fatemi, S. Fang, K. Watanabe, T. Taniguchi, E. Kaxiras, P. Jarillo-Herrero, Unconventional superconductivity in magic-angle graphene superlattices, Nature 556 (2018) 43–50, https://doi.org/10.1038/nature26160.

[15] I. Hagymási, M.S. Mohd Isa, Z. Tajkov, K. Márity, L. Oroszlány, J. Koltai, A. Alassaf, P. Kun, K. Kandrai, A. Pálinkás, P. Vancsó, L. Tapasztó, P. Nemes-Incze, Observation of competing, correlated ground states in the flat band of rhombohedral graphite, Sci. Adv. 8 (2022) eabo6879, https://doi.org/10.1126/sciadv.abo6879.

[16] Y. Shi, S. Xu, Y. Yang, S. Slizovskiy, S.V. Morozov, S.K. Son, S. Ozdemir, C. Mullan, J. Barrier, J. Yin, A.I. Berdyugin, B.A. Piot, T. Taniguchi, K. Watanabe, V.I. Fal'ko, K.S. Novoselov, A.K. Geim, A. Mishchenko, Electronic phase separation in multilayer rhombohedral graphite, Nature 584 (2020) 210–214, https://doi.org/10.1038/s41586-020-2568-2.

[17] R. Bistritzer, A.H. MacDonald, Moiré bands in twisted double-layer graphene, Proc. Natl. Acad. Sci. U.S.A 108 (2011) 12233–12237, https://doi.org/10.1073/pnas.1108174108.

[18] M.D. Bhatt, H. Kim, G. Kim, Various defects in graphene: a review, RSC Adv 12 (2022) 21520–21547, https://doi.org/10.1039/d2ra01436j.

[19] L. Fan, J. Xu, Y. Hong, Defects in graphene-based heterostructures: topological and geometrical effects, RSC Adv 12 (2022) 6772–6782, https://doi.org/10.1039/d1ra08884j.
[20] B.M. Garraway, K.A. Suominen, Wave-packet dynamics: new physics and chemistry in femto-time, Rep. Prog. Phys. 58 (1995) 365, https://doi.org/10.1088/0034-4885/58/4/001.
[21] P. Vancsó, G.I. Márk, Ph. Lambin, A. Mayer, Y.S. Kim, C. Hwang, L.P. Biró, Electronic transport through ordered and disordered graphene grain boundaries, Carbon N Y 64 (2013) 101–110, https://doi.org/10.1016/j.carbon.2013.07.041.
[22] G.I. Márk, P. Vancsó, C. Hwang, Ph. Lambin, L.P. Biró, Anisotropic dynamics of charge carriers in graphene, Phys. Rev. B 85 (2012), 125443, https://doi.org/10.1103/PhysRevB.85.125443.
[23] P. Vancsó, A. Mayer, P. Nemes-Incze, G.I. Márk, Wave packet dynamical simulation of quasiparticle interferences in 2D, Materials, Appl. Sci. 11 (2021) 4730, https://doi.org/10.3390/app11114730.
[24] H.N. Do, H.A. Le, D. Bercioux, Time-evolution patterns of electrons in twisted bilayer graphene, Phys. Rev. B 99 (2019), 165127, https://doi.org/10.1103/PhysRevB.99.165127.
[25] A. Mayer, Band structure and transport properties of carbon nanotubes using a local pseudopotential and a transfer-matrix technique, Carbon N Y 42 (2004) 2057–2066, https://doi.org/10.1016/j.carbon.2004.04.017.
[26] P. Vancsó, G.I. Márk, Ph. Lambin, A. Mayer, C. Hwang, L.P. Biró, Effect of the disorder in graphene grain boundaries: a wave packet dynamics study, Appl. Surf. Sci. 291 (2014) 58–63, https://doi.org/10.1016/j.apsusc.2013.09.127.
[27] D.G. Kvashnin, P. Vancsó, L.Y. Antipina, G.I. Márk, L.P. Biró, P.B. Sorokin, L. A. Chernozatonskii, Bilayered semiconductor graphene nanostructures with periodically arranged hexagonal holes, Nano Res 8 (2015) 1250–1258, https://doi.org/10.1007/s12274-014-0611-z.
[28] Y. Wang, K. Scheerschmidt, U. Gösele, Theoretical investigations of bond properties in graphite and graphitic silicon, Phys. Rev. B 61 (2000) 12864–12870, https://doi.org/10.1103/PhysRevB.61.12864.
[29] J.C. Charlier, X. Gonze, J.P. Michenaud, First-principles study of the stacking effect on the electronic properties of graphite(s), Carbon N Y 32 (1994) 289–299, https://doi.org/10.1016/0008-6223(94)90192-9.
[30] Y. Fukaya, Y. Zhao, H.W. Kim, J.R. Ahn, H. Fukidome, I. Matsuda, Atomic arrangements of quasicrystal bilayer graphene: interlayer distance expansion, Phys. Rev. B 104 (2021), L180202, https://doi.org/10.1103/PhysRevB.104.L180202.
[31] V.N. Do, Proof for the electronic band crossing in sliding bilayer graphene, Phys. Rev. B 104 (2021), 205121, https://doi.org/10.1103/PhysRevB.104.205121.
[32] F. Zhang, B. Sahu, H. Min, A.H. MacDonald, Band structure of ABC-stacked graphene trilayers, Phys. Rev. B 82 (2010), 035409, https://doi.org/10.1103/PhysRevB.82.035409.
[33] T.M. Rusin, W. Zawadzki, Transient Zitterbewegung of charge carriers in mono- and bilayer graphene, and carbon nanotubes, Phys. Rev. B 76 (2007), 195439, https://doi.org/10.1103/PhysRevB.76.195439.
[34] W.P. Su, J.R. Schrieffer, A.J. Heeger, Solitons in polyacetylene, Phys. Rev. Lett. 42 (1979) 1698–1701, https://doi.org/10.1103/PhysRevLett.42.1698.
[35] L. Xian, Z.F. Wang, M.Y. Chou, Coupled dirac fermions and neutrino-like oscillations in twisted bilayer graphene, Nano Lett 13 (2013) 5159–5164, https://doi.org/10.1021/nl4024403.